PHILOSOPHICAL TRANSACTIONS OF THE ROYAL SOCIETY A MATHEMATICAL, PHYSICAL & ENGINEERING SCIENCES

# The role of disc-type crystal shape for micromechanical predictions of elasticity and strength of hydroxyapatite biomaterials

Andreas Fritsch, Christian Hellmich and Luc Dormieux

*Phil. Trans. R. Soc. A* 2010 **368**, 1913-1935
doi: 10.1098/rsta.2010.0005

PHILOSOPHICAL TRANSACTIONS OF THE ROYAL SOCIETY A

*Phil. Trans. R. Soc. A* (2010) **368**, 1913–1935
doi:10.1098/rsta.2010.0005

# The role of disc-type crystal shape for micromechanical predictions of elasticity and strength of hydroxyapatite biomaterials

By Andreas Fritsch[1], Christian Hellmich[1,*] and Luc Dormieux[2]

[1]*Institute for Mechanics of Materials and Structures, Vienna University of Technology (TU Wien), 1040 Vienna, Austria*
[2]*École des Ponts Paris Tech, 77455 Marne-la-Vallée, France*

The successful design of ceramic bone biomaterials is challenged by two competing requirements: on the one hand, such materials need to be stiff and strong, which would suggest a low porosity (of pore sizes in the 10–100 µm range) to be targeted; on the other hand, bone biomaterials need to be bioactive (in particular vascularized), which suggests a high porosity of such materials. Conclusively, reliable information on how porosity drives the stiffness and strength properties of ceramic bone biomaterials (tissue engineering scaffolds) is of great interest. In this context, mathematical models are increasingly being introduced into the field. Recently, self-consistent continuum micromechanics formulations have turned out as expressedly efficient and reliable tools to predict hydroxyapatite biomaterials' stiffness and strength, as a function of the biomaterial-specific porosity, and of the 'universal' properties of the individual hydroxyapatite crystals: their stiffness, strength and shape. However, the precise crystal shape can be suitably approximated by specific ellipsoidal shapes: while it was shown earlier that spherical shapes do not lead to satisfactory results, and that acicular shapes are an appropriate choice, we here concentrate on disc-type crystal shape as, besides needles, plates are often reported in micrographs of hydroxyapatite biomaterials. Disc-based model predictions of a substantial set of experimental data on stiffness and strength of hydroxyapatite biomaterials almost attain the quality of the very satisfactory needle-based models. This suggests that, as long as the crystal shape is clearly non-spherical, its precise shape is of secondary importance if stiffness and strength of hydroxyapatite biomaterials are predicted on the basis of continuum micromechanics, from their micromorphology and porosity.

**Keywords: micromechanics; hydroxyapatite; disc; needle; strength; elasticity**

## 1. Introduction

The successful design of ceramic bone biomaterials is challenged by two competing requirements (Pereira *et al.* 2005; Cancedda *et al.* 2007): on the one hand, such materials need to be stiff and strong, which would suggest a low porosity (of pore

*Author for correspondence (christian.hellmich@tuwien.ac.at).

One contribution of 14 to a Theme Issue 'Advanced processing of biomaterials'.

 

Table 1. Nomenclature.

| | |
|---|---|
| $\mathbb{A}_r$ | fourth-order strain concentration tensor of phase $r$ |
| $\mathbb{A}_r^{\mathrm{est}}$ | estimate of fourth-order strain concentration tensor of phase $r$ |
| $\mathbb{B}_{\mathrm{HA}}$ | fourth-order stress concentration tensor for HA crystal phases |
| $\mathbb{C}$ | fourth-order homogenized stiffness tensor |
| $\mathbb{C}^{\mathrm{est}}$ | estimate of fourth-order homogenized stiffness tensor |
| $\mathbb{C}^0$ | fourth-order stiffness tensor of infinite matrix surrounding an ellipsoidal inclusion |
| $\mathbb{C}_{\mathrm{poly}}$ | fourth-order homogenized stiffness tensor of biomaterial made of HA |
| $\mathbb{c}_{\mathrm{HA}}$ | fourth-order stiffness tensor of single HA crystals within the RVE $V_{\mathrm{poly}}$ |
| $\mathbb{c}_r$ | fourth-order stiffness tensor of phase $r$ |
| $d$ | characteristic length of inhomogeneity within an RVE |
| $\boldsymbol{E}$ | second-order macroscopic strain tensor |
| $E_{\mathrm{exp}}$ | experimental Young's modulus of biomaterial made of HA |
| $E_{\mathrm{HA}}$ | Young's modulus of single HA crystals within the RVE $V_{\mathrm{poly}}$ |
| $E_{\mathrm{poly}}$ | homogenized Young's modulus of biomaterial made of HA |
| $\bar{\mathcal{E}}$ | mean of absolute error between model predictions and experiments |
| $\mathcal{E}_S$ | standard deviation of relative error between model predictions and experiments |
| $\bar{e}$ | normalized mean error between model predictions and experiments ('relative error measure') |
| $e_S$ | normalized standard deviation of errors between model predictions and experiments |
| $\underline{e}_1$, $\underline{e}_2$, $\underline{e}_3$ | unit base vectors of Cartesian reference base frame |
| $\underline{e}'_1$, $\underline{e}'_2$, $\underline{e}'_3$ | unit base vectors of Cartesian local base frame for shear failure definition |
| $\underline{e}_\vartheta$, $\underline{e}_\varphi$, $\underline{e}_r$ | unit base vectors of Cartesian local (spherical) base frame attached to disc |
| $\mathfrak{F}(\boldsymbol{\Sigma})$ | boundary of elastic domain in space of macrostresses |
| $f$ | ultrasonic excitation frequency |
| $f_r$ | volume fraction of phase $r$ |
| $\mathfrak{f}_r(\boldsymbol{\sigma}_r)$ | boundary of elastic domain of phase $r$ in space of microstresses |
| HA | hydroxyapatite |
| $\mathbb{I}$ | fourth-order identity tensor |
| $\mathbb{J}$ | volumetric part of fourth-order identity tensor $\mathbb{I}$ |
| $\mathbb{K}$ | deviatoric part of fourth-order identity tensor $\mathbb{I}$ |
| $k_{\mathrm{HA}}$ | bulk modulus of single HA crystals within the RVE $V_{\mathrm{poly}}$ |
| $k_{\mathrm{poly}}$ | homogenized bulk modulus of biomaterial made of HA |
| $\mathcal{L}$ | characteristic length of a structure built up by material RVEs |
| $\ell$ | characteristic length of RVEs |
| $M$ | mass of an HA biomaterial sample |
| $\underline{N}$ | vector within the plane of one disc-type crystal phase |
| $N_r$ | number of phases within an RVE |
| $\underline{n}$ | vector perpendicular to $\underline{N}$ |
| $\mathbb{P}_r^0$ | fourth-order Hill tensor characterizing the interaction between the phase $r$ and the matrix $\mathbb{C}^0$ |
| $\mathbb{P}_{\mathrm{disc}}^{\mathrm{poly}}$ | fourth-order Hill tensor for disc-like inclusion in matrix with stiffness $\mathbb{C}_{\mathrm{poly}}$ |
| $\mathbb{P}_{\mathrm{sph}}^{\mathrm{poly}}$ | fourth-order Hill tensor for spherical inclusion in matrix with stiffness $\mathbb{C}_{\mathrm{poly}}$ |
| $\bar{q}_{\mathrm{exp}}$ | mean value of experimental data |
| RVE | representative volume element |
| $r$, $s$ | index for phases |
| $\mathbb{S}_r^{\mathrm{esh},0}$ | fourth-order Eshelby tensor for phase $r$ embedded in matrix $\mathbb{C}^0$ |
| $\mathbb{S}_{\mathrm{disc}}^{\mathrm{esh}}$ | fourth-order Eshelby tensor for disc-like inclusion embedded in isotropic matrix with stiffness $\mathbb{C}_{\mathrm{poly}}$ |
| $\mathbb{S}_{\mathrm{sph}}^{\mathrm{esh}}$ | fourth-order Eshelby tensor for spherical inclusion embedded in isotropic matrix with stiffness $\mathbb{C}_{\mathrm{poly}}$ |

(*Continued.*)

Table 1. (*Continued.*)

| | |
|---|---|
| tr | trace of a second-order tensor |
| $V$ | volume of an HA biomaterial sample |
| $V_{\mathrm{RVE}}$ | volume of an RVE |
| $v$ | ultrasonic wave propagation velocity within an HA biomaterial sample |
| $w$ | index denoting weakest phase |
| $\underline{x}$ | position vector within an RVE |
| $\beta$ | ratio between uniaxial tensile strength and shear strength of pure HA |
| $\delta_{ij}$ | Kronecker delta (components of second-order identity tensor $\mathbf{1}$) |
| $\boldsymbol{\varepsilon}_{\mathrm{HA}}$ | second-order strain tensor field within single HA crystals |
| $\boldsymbol{\varepsilon}_r$ | second-order strain tensor field of phase $r$ |
| $\vartheta$ | latitudinal coordinate of spherical disc-specific coordinate system ($\underline{e}_\vartheta$, $\underline{e}_\varphi$, $\underline{e}_r$) |
| $\vartheta'$ | latitudinal coordinate of local shear failure-defining coordinate system ($\underline{e}'_1, \underline{e}'_2, \underline{e}'_3$) |
| $\lambda$ | ultrasonic wavelength |
| $\mu_{\mathrm{HA}}$ | shear modulus of single HA crystals within the RVE $V_{\mathrm{poly}}$ |
| $\mu_{\mathrm{poly}}$ | homogenized shear modulus of biomaterial made of HA |
| $\nu_{\mathrm{exp}}$ | experimental Poisson's ratio of biomaterial made of HA |
| $\nu_{\mathrm{HA}}$ | Poisson's ratio of single HA crystals within the RVE $V_{\mathrm{poly}}$ |
| $\nu_{\mathrm{poly}}$ | homogenized Poisson's ratio of biomaterial made of HA |
| $\underline{\xi}$ | displacements within an RVE and at its boundary |
| $\rho_{\mathrm{HA}}$ | mass density of pure HA |
| $\rho_{\mathrm{s}}$ | mass density of an HA biomaterial sample |
| $\boldsymbol{\Sigma}$ | second-order macroscopic stress tensor |
| $\Sigma_{\mathrm{poly}}^{\mathrm{ult,t}}$ | model-predicted uniaxial tensile strength of biomaterial made of HA |
| $\Sigma_{\mathrm{poly}}^{\mathrm{ult,c}}$ | model-predicted uniaxial compressive strength of biomaterial made of HA |
| $\Sigma_{\mathrm{exp}}^{\mathrm{ult,t}}$ | experimental uniaxial tensile strength of biomaterial made of HA |
| $\Sigma_{\mathrm{exp}}^{\mathrm{ult,c}}$ | experimental uniaxial compressive strength of biomaterial made of HA |
| $\Sigma_{\mathrm{ref}}$ | component of uniaxial stress tensor $\boldsymbol{\Sigma}$ imposed on boundary of biomaterial made of HA |
| $\boldsymbol{\sigma}_{\mathrm{HA}}(\varphi, \vartheta)$ | second-order stress tensor within disc-type HA crystal phases |
| $\sigma_{\mathrm{HA},NN}(\varphi, \vartheta; \psi)$ | normal component of stress tensor $\boldsymbol{\sigma}_{\mathrm{HA}}(\varphi, \vartheta)$ in direction $\underline{N}$ |
| $\sigma_{\mathrm{HA},Nn}$ $(\varphi, \vartheta; \psi; \omega)$ | shear component of stress tensor $\boldsymbol{\sigma}_{\mathrm{HA}}(\varphi, \vartheta)$ acting in planes orthogonal to the disc plane |
| $\sigma_{\mathrm{HA}}^{\mathrm{ult,t}}$ | uniaxial tensile strength of pure HA |
| $\sigma_{\mathrm{HA}}^{\mathrm{ult,s}}$ | shear strength of pure HA |
| $\boldsymbol{\sigma}_r$ | second-order stress tensor averaged over phase $r$ |
| $\varphi$ | longitudinal coordinate of spherical disc-specific coordinate system ($\underline{e}_\vartheta, \underline{e}_\varphi, \underline{e}_r$) |
| $\varphi'$ | longitudinal coordinate of local shear failure-defining coordinate system ($\underline{e}'_1, \underline{e}'_2, \underline{e}'_3$) |
| $\phi$ | volume fraction of pores within RVE of porous HA biomaterial |
| $\psi$ | angle defining vector $\underline{N}$ in $\underline{e}_\vartheta$, $\underline{e}_\varphi$-plane |
| $\omega$ | angle defining vector $\underline{n}$ in $\underline{e}'_1$, $\underline{e}'_2$-plane |
| $\partial V$ | boundary of an RVE |
| $\mathbf{1}$ | second-order identity tensor |
| $\langle(\cdot)\rangle_V =$ $1/V \int_V (\dot{}) \mathrm{d}V$ | average of quantity (.) over volume $V$ |
| $\cdot$ | first-order tensor contraction |
| : | second-order tensor contraction |
| $\otimes$ | dyadic product of tensors |

sizes in the 10–100 μm range) to be targeted; on the other hand, bone biomaterials need to be bioactive (in particular vascularized), which suggests a high porosity of such materials. Conclusively, reliable information on how porosity drives the stiffness and strength properties of ceramic bone biomaterials (tissue engineering scaffolds) is of great interest, and as exploration of porosity–mechanical property relationships on a purely experimental basis is likely to become laborious and uneconomic, mathematical models are increasingly being introduced into the field. Most of them rely on computer tomography (CT) in combination with the finite element (FE) method, relying on reasonably guessed homogeneous material properties for the bulk phase (Lacroix *et al.* 2006), or on X-ray physics-based and micromechanics-derived inhomogeneous material properties (Scheiner *et al.* 2009). However, such approaches aim at translation of comprehensive CT-based geometrical information, rather than at predicting mechanical properties for porosities which have not yet been realized (and CT scanned). Also, such approaches are typically restricted to the linear elastic regime of material behaviour (FE-based biomaterial strength predictions are rarely documented—if at all).

Quite recently, continuum micromechanics formulations (Hill 1963; Zaoui 2002) have turned out as a valuable alternative for predicting porosity–mechanical property relationships on the basis of microstructural mechanical interactions in ceramic bone biomaterials (Fritsch *et al.* 2007, 2009; Malasoma *et al.* 2008): such models do not resolve all details of the materials' microstructure (which, as a rule, are not known anyway), but consider essential morphological features (shapes) of homogeneous subdomains (phases) within a representative volume element (RVE) of the investigated biomaterial. In our case, both the intercrystalline pores and the ceramic crystals are modelled as ellipsoidal inclusions in an infinite matrix with stiffness properties of the overall biomaterial (self-consistent approach; Hershey 1954; Kröner 1958). This matrix is subjected to strains at infinity which—thanks to the Eshelby–Laws solutions (Eshelby 1957; Laws 1977)—can be semi-analytically related to the strains in the ellipsoidal inclusions. The aforementioned strains at infinity are chosen such that the spatial average of the pore and crystal (inclusion) strains are identical to the strains which are subjected homogeneously to the boundary of an RVE of the considered biomaterial, in order to mimic the fact that the spatial average of any kinematically compatible (real) strain field within the RVE is identical to homogeneous (macroscopic) strains at the RVE's boundary. This leads to semi-analytical expressions for the biomaterial's stiffness, as a function of the biomaterial's porosity and of the crystal stiffnesses (and depending on their shape), but also for the concentration tensors relating the macroscopic strains to the phase strains. The latter allow for relating the crystal strains associated with brittle crystal failure to the corresponding overall macroscopic strain states related to the biomaterial's failure—hence, they allow for predicting the biomaterial's strength as a function of the biomaterial's porosity, as well as of the single crystals' stiffness, strength and shape.

While it was known for a while that the traditional assumption of simply considering spherical phase shape for the crystals neither allows for biomaterial stiffness predictions of low porosity materials, nor for strength predictions at any porosity (which has led to the premature conclusion that continuum micromechanics approaches might be generally too 'crude' for modelling biomaterials), it turned out recently that consideration of non-spherical crystal shapes oriented in all space orientations does deliver very satisfactory elasticity

and strength predictions of brittle biomaterials based on hydroxyapatite (HA). Specifically, this was shown for needle-type crystals (Fritsch *et al.* 2009). However, while it is understood that the considered crystal shape needs to be non-spherical, the question arises whether the shape necessarily needs to be acicular, in particular given the fact that, in micrographs, the crystals sometimes appear to be more plate-shaped. The present paper aims at contributing to answer this question, by developing a micromechanics representation based on coin-shaped ceramic crystals, and comparing the model predictions both to experiments and to predictions of needle-based representations.

After recalling the fundamentals of continuum micromechanics (§2), we describe a disc-shape-based micromechanical representation of porous HA biomaterials for predicting these materials' elastic and strength properties (§3). To assess the quality of such predictions, the model is then carefully validated against experimental results (§4). Finally, typical model features are discussed—and compared with our earlier results (Fritsch *et al.* 2009) based on needle-type crystal morphology.

## 2. Fundamentals of continuum micromechanics

### (*a*) *RVE and phase properties*

In continuum micromechanics (Hill 1963; Hashin 1983; Suquet 1997; Zaoui 2002), a material is understood as a macrohomogeneous, but microheterogeneous body filling an RVE with characteristic length $\ell$, $\ell \gg d$, $d$ standing for the characteristic length of inhomogeneities within the RVE, and $\ell \ll \mathcal{L}$, $\mathcal{L}$ standing for the characteristic lengths of geometry or loading of a structure built up by the material defined on the RVE (figure 1). Table 1 contains all mathematical symbols and abbreviations used throughout the article. In general, the microstructure within one RVE is so complicated that it cannot be described in complete detail. Therefore, $N_r$ quasi-homogeneous subdomains with known physical quantities are reasonably chosen. They are called material phases (figure 1*a*).

Quantitative phase properties are volume fractions $f_r$ of phases $r = 1, \ldots, N_r$, as well as elastic and strength properties of phases. As regards phase elasticity, the fourth-order stiffness tensor $\mathbb{c}_r$ relates the (average microscopic) second-order strain tensor in phase $r$, $\boldsymbol{\varepsilon}_r$, to the (average microscopic) second-order stress tensor in phase $r$, $\boldsymbol{\sigma}_r$,

$$\boldsymbol{\sigma}_r = \mathbb{c}_r : \boldsymbol{\varepsilon}_r. \tag{2.1}$$

As regards phase strength, brittle failure can be associated to the boundary of an elastic domain $\mathfrak{f}_r(\boldsymbol{\sigma}) < 0$,

$$\mathfrak{f}_r(\boldsymbol{\sigma}) = 0 \tag{2.2}$$

defined in the space of microstresses $\boldsymbol{\sigma}(\underline{x})$, $\underline{x}$ being the position vector for locations within or at the boundary of the RVE.

Also, the spatial arrangement of the phases needs to be specified. In this respect, two cases are of particular interest: (i) one or several inclusion phases with different shapes are embedded in a contiguous 'matrix' phase (as in a reinforced composite material) or (ii) mutual contact of all disorderly arranged phases (as in a polycrystal).

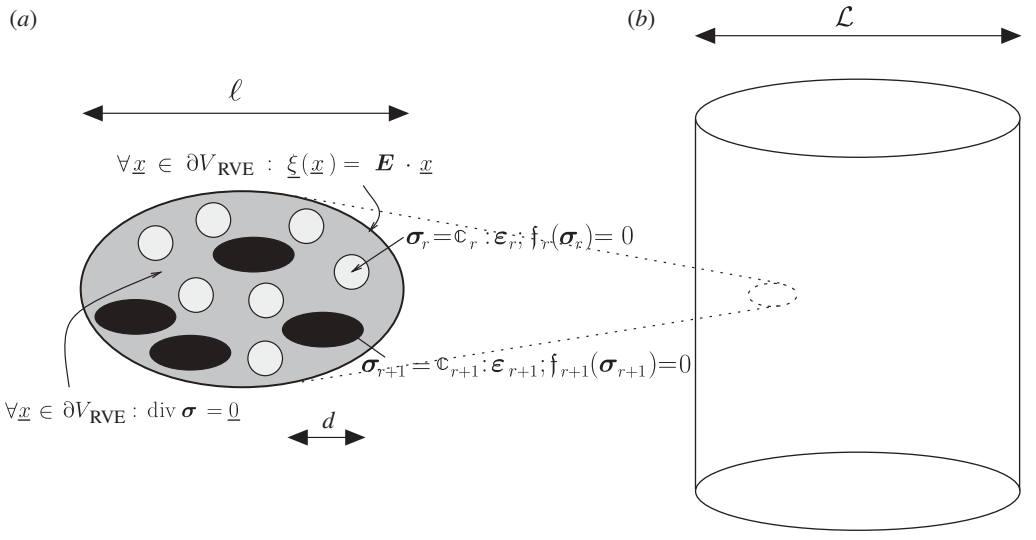


Figure 1. (*a*) Loading of an RVE, built up by phases $r$ with stiffness $\mathbb{C}_r$ and strength properties $\mathfrak{f}_r(\boldsymbol{\sigma}_r) = 0$, according to continuum micromechanics (Hashin 1983; Zaoui 2002): displacements $\underline{\xi}$, related to a constant (homogenized) strain $\boldsymbol{E}$, are imposed at the boundary of the RVE; (*b*) structure built up of material defined on RVE (*a*).

### (*b*) *Averaging—homogenization*

The central goal of continuum micromechanics is to estimate the mechanical properties (such as elasticity or strength) of the material defined on the RVE (the macrohomogeneous, but microheterogeneous medium) from the aforementioned phase properties. This procedure is referred to as homogenization or one homogenization step. Therefore, homogeneous (macroscopic) strains $\boldsymbol{E}$ are imposed onto the RVE, in terms of displacements at its boundary $\partial V$:

$$\forall \underline{x} \in \partial V : \underline{\xi}(\underline{x}) = \boldsymbol{E} \cdot \underline{x}. \tag{2.3}$$

As a consequence, the resulting kinematically compatible microstrains $\boldsymbol{\varepsilon}(\underline{x})$ throughout the RVE with volume $V_{\mathrm{RVE}}$ fulfil the average condition (Hashin 1983),

$$\boldsymbol{E} = \langle \boldsymbol{\varepsilon} \rangle = \frac{1}{V_{\mathrm{RVE}}} \int_{V_{\mathrm{RVE}}} \boldsymbol{\varepsilon}\, \mathrm{d}V = \sum_r f_r \boldsymbol{\varepsilon}_r \tag{2.4}$$

providing a link between micro- and macrostrains. Analogously, homogenized (macroscopic) stresses $\boldsymbol{\Sigma}$ are defined as the spatial average over the RVE, of the microstresses $\boldsymbol{\sigma}(\underline{x})$,

$$\boldsymbol{\Sigma} = \langle \boldsymbol{\sigma} \rangle = \frac{1}{V_{\mathrm{RVE}}} \int_{V_{\mathrm{RVE}}} \boldsymbol{\sigma}\, \mathrm{d}V = \sum_r f_r \boldsymbol{\sigma}_r. \tag{2.5}$$

Homogenized (macroscopic) stresses and strains, $\boldsymbol{\Sigma}$ and $\boldsymbol{E}$, are related by the homogenized (macroscopic) stiffness tensor $\mathbb{C}$,

$$\boldsymbol{\Sigma} = \mathbb{C} : \boldsymbol{E}, \tag{2.6}$$

which needs to be linked to the stiffnesses $\mathbb{c}_r$, the shape and the spatial arrangement of the phases (§2*a*). This link is based on the linear relation between the homogenized (macroscopic) strain $\boldsymbol{E}$ and the average (microscopic) strain $\boldsymbol{\varepsilon}_r$, resulting from the superposition principle valid for linear elasticity, see equation (2.1) (Hill 1963). This relation is expressed in terms of the fourth-order concentration tensors $\mathbb{A}_r$ of each of the phases $r$

$$\boldsymbol{\varepsilon}_r = \mathbb{A}_r : \boldsymbol{E}. \tag{2.7}$$

Insertion of equation (2.7) into equation (2.1) and averaging over all phases according to equation (2.5) leads to

$$\boldsymbol{\Sigma} = \sum_r f_r \mathbb{c}_r : \mathbb{A}_r : \boldsymbol{E}. \tag{2.8}$$

From equations (2.8) and (2.6), we can identify the sought relation between the phase stiffness tensors $\mathbb{c}_r$ and the overall homogenized stiffness $\mathbb{C}$ of the RVE,

$$\mathbb{C} = \sum_r f_r \mathbb{c}_r : \mathbb{A}_r. \tag{2.9}$$

The concentration tensors $\mathbb{A}_r$ can be suitably estimated from Eshelby's (1957) matrix–inclusion problem, relating the strains in an ellipsoidal inclusion surrounded by an infinite matrix of stiffness $\mathbb{C}^0$ to the strains $\boldsymbol{E}^0$ imposed at infinity to the latter matrix. Approximating the strains in all phases $r$ by such inclusion strains (as sketched in figure 3 for the considered HA biomaterials) delivers

$$\boldsymbol{\varepsilon}_r = \left[\mathbb{I} + \mathbb{P}_r^0 : (\mathbb{c}_r - \mathbb{C}^0)\right]^{-1} : \boldsymbol{E}^0, \tag{2.10}$$

where $\mathbb{I}$, $I_{ijkl} = 1/2(\delta_{ik}\delta_{jl} + \delta_{il}\delta_{kj})$, is the fourth-order unity tensor, $\delta_{ij}$ (Kronecker delta) are the components of second-order identity tensor $\mathbf{1}$, and the fourth-order Hill tensor $\mathbb{P}_r^0$ accounts for the shape of phase $r$, represented as an ellipsoidal inclusion embedded in a fictitious matrix of stiffness $\mathbb{C}^0$. For isotropic matrices (which is the case considered throughout this article), $\mathbb{P}_r^0$ is accessible via the Eshelby (1957) tensor

$$\mathbb{S}_r^{\mathrm{esh},0} = \mathbb{P}_r^0 : \mathbb{C}^0 \tag{2.11}$$

(see also §3). Insertion of equation (2.10) into equation (2.4) allows for expression of $\boldsymbol{E}^0$ in terms of $\boldsymbol{E}$, and re-insertion of this result into equation (2.10) delivers the sought estimate for the strain concentration tensor as (Benveniste 1987; Zaoui 2002)

$$\mathbb{A}_r^{\mathrm{est}} = \left[\mathbb{I} + \mathbb{P}_r^0 : (\mathbb{c}_r - \mathbb{C}^0)\right]^{-1} : \left\{\sum_s f_s \left[\mathbb{I} + \mathbb{P}_s^0 : (\mathbb{c}_s - \mathbb{C}^0)\right]^{-1}\right\}^{-1}. \tag{2.12}$$

Backsubstitution of equation (2.12) into equation (2.9) delivers the sought estimate for the homogenized (macroscopic) stiffness tensor, $\mathbb{C}^{\mathrm{est}}$, as

$$\mathbb{C}^{\mathrm{est}} = \sum_r f_r \mathbb{c}_r : \left[\mathbb{I} + \mathbb{P}_r^0 : (\mathbb{c}_r - \mathbb{C}^0)\right]^{-1} : \left\{\sum_s f_s \left[\mathbb{I} + \mathbb{P}_s^0 : (\mathbb{c}_s - \mathbb{C}^0)\right]^{-1}\right\}^{-1}. \tag{2.13}$$

Choice of matrix stiffness $\mathbb{C}^0$ determines which type of interactions between the phases is considered: for $\mathbb{C}^0$ coinciding with one of the phase stiffnesses (Mori–Tanaka scheme; Mori & Tanaka 1973), a composite material is represented (contiguous matrix with inclusions); for $\mathbb{C}^0 = \mathbb{C}^{\mathrm{est}}$ (self-consistent scheme; Hershey 1954; Kröner 1958), a dispersed arrangement of the phases is considered (typical for polycrystals).

As long as the average phase strains $\boldsymbol{\varepsilon}_r$ are relevant for brittle phase failure, resulting in overall failure of the RVE, concentration relation (2.7) allows for translation of the brittle failure criterion of the weakest phase $r = w$ into a macroscopic (homogenized) brittle failure criterion, according to equations (2.1), (2.2), (2.6) and (2.7),

$$\mathfrak{f}_w(\boldsymbol{\sigma}) = 0 = \mathfrak{f}_w(\mathbb{c}_w : \boldsymbol{\varepsilon}_w) = \mathfrak{f}_w(\mathbb{c}_w : \mathbb{A}_w : \boldsymbol{E}) = \mathfrak{f}_w(\mathbb{c}_w : \mathbb{A}_w : \mathbb{C}^{-1} : \boldsymbol{\Sigma}) = \mathfrak{F}(\boldsymbol{\Sigma}). \tag{2.14}$$

Fourth-order tensor operations such as the ones occurring in equations (2.1) and (2.6)–(2.13) can be suitably evaluated in a vector/matrix-based software, through a compressed vector/matrix notation with normalized tensorial basis, often referred to as the Kelvin or the Mandel notation, see Cowin & Mehrabadi (1992), Cowin (2003) and Helnwein (2001) for details.

## 3. Micromechanical representation of porous HA biomaterials, based on disc-shaped crystals—stiffness and strength estimates

In the line of the concept presented in §2, we envision biomaterials made of HA as porous polycrystals consisting of (i) discs or coins (a coin being the limit case of an oblate inclusion) with stiffness $\mathbb{c}_{\mathrm{HA}}$ and volume fraction $(1-\phi)$, being oriented in all space directions, and of (ii) spherical (empty) pores with vanishing stiffness and volume fraction $\phi$ (porosity; see figures 2 and 3).

### (a) *Stiffness estimate*

In a reference frame $(\underline{e}_1, \underline{e}_2, \underline{e}_3)$, the HA disc orientation vector $\underline{e}_r$ (normal vector of the disc) is given by Euler angles $\vartheta$ and $\varphi$ (figure 2). Specification of equation (2.13) for $\mathbb{C}^0 = \mathbb{C}^{\mathrm{est}} = \mathbb{C}_{\mathrm{poly}}$ (self-consistent scheme) and for an infinite number of solid phases related to orientation directions $\underline{e}_r(\vartheta, \varphi)$, which are uniformly distributed in space ($\varphi \in [0, 2\pi]; \vartheta \in [0, \pi]$), yields the homogenized stiffness of the porous HA biomaterial depicted in figure 3 (Fritsch *et al.* 2006)

$$\mathbb{C}_{\mathrm{poly}} = (1-\phi)\mathbb{c}_{\mathrm{HA}} : \left\langle \left[ \mathbb{I} + \mathbb{P}^{\mathrm{poly}}_{\mathrm{disc}} : (\mathbb{c}_{\mathrm{HA}} - \mathbb{C}_{\mathrm{poly}}) \right]^{-1} \right\rangle : \left\{ (1-\phi) \left\langle \left[ \mathbb{I} + \mathbb{P}^{\mathrm{poly}}_{\mathrm{disc}} : (\mathbb{c}_{\mathrm{HA}} - \mathbb{C}_{\mathrm{poly}}) \right]^{-1} \right\rangle + \phi \left( \mathbb{I} - \mathbb{P}^{\mathrm{poly}}_{\mathrm{sph}} : \mathbb{C}_{\mathrm{poly}} \right)^{-1} \right\}^{-1} \tag{3.1}$$

with the angular average

$$\left\langle \left[ \mathbb{I} + \mathbb{P}^{\mathrm{poly}}_{\mathrm{disc}} : (\mathbb{c}_{\mathrm{HA}} - \mathbb{C}_{\mathrm{poly}}) \right]^{-1} \right\rangle = \int_{\varphi=0}^{2\pi} \int_{\vartheta=0}^{\pi} \left[ \mathbb{I} + \mathbb{P}^{\mathrm{poly}}_{\mathrm{disc}}(\vartheta, \varphi) : (\mathbb{c}_{\mathrm{HA}} - \mathbb{C}_{\mathrm{poly}}) \right]^{-1} \times \frac{\sin\vartheta \, \mathrm{d}\vartheta \, \mathrm{d}\varphi}{4\pi}, \tag{3.2}$$

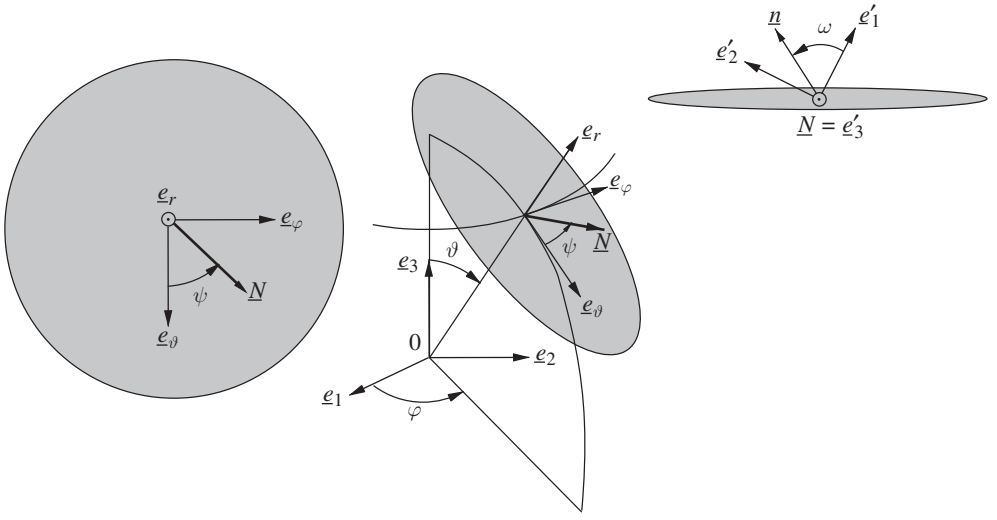


Figure 2. Disc-like representation of HA crystals with normals oriented along vector $\underline{e}_r$, inclined by Euler angles $\vartheta$ and $\varphi$ with respect to the reference frame ($\underline{e}_1$, $\underline{e}_2$, $\underline{e}_3$); local base frame ($\underline{e}_r$, $\underline{e}_\varphi$, $\underline{e}_\vartheta$) is attached to the disc; another local frame ($\underline{e}'_1$, $\underline{e}'_2$, $\underline{e}'_3$) is introduced for definition of the shear stress direction (see appendix A for more details).

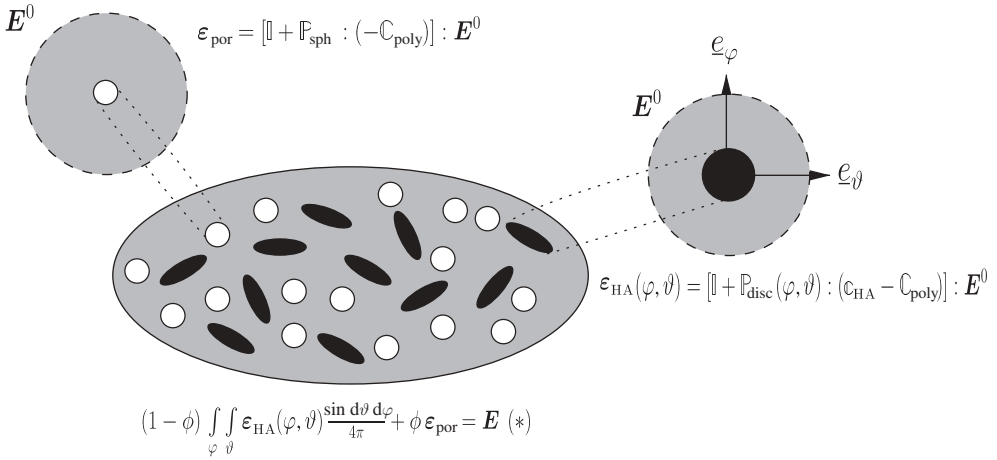


Figure 3. Self-consistent phase interaction within RVE of porous biomaterial made of HA: uniform orientation distribution of oblate (disc-like) HA inclusions (with stiffness $\mathbb{c}_{\mathrm{HA}}$ and volume fraction $(1-\phi)$) and spherical (empty) pores (with zero stiffness and volume fraction $\phi$), in fictitious infinite matrix with stiffness $\mathbb{C}_{\mathrm{poly}}$ of overall porous polycrystal and vanishing volume fraction, subjected at infinity to homogeneous strains $\boldsymbol{E}^0$, such that strain average rule (*), see also equation (2.4), is fulfilled.

where $\mathbb{P}^{\mathrm{poly}}_{\mathrm{sph}}$ and $\mathbb{P}^{\mathrm{poly}}_{\mathrm{disc}}$ are the fourth-order Hill tensors for spherical and disc-like inclusions, respectively, in an isotropic matrix with stiffness $\mathbb{C}_{\mathrm{poly}} = 3k_{\mathrm{poly}}\mathbb{J} + 2\mu_{\mathrm{poly}}\mathbb{K}$; $\mathbb{J}$, $J_{ijkl} = 1/3\delta_{ij}\delta_{kl}$, is the volumetric part of the fourth-order unity tensor

$\mathbb{I}$, and $\mathbb{K}=\mathbb{I}-\mathbb{J}$ is its deviatoric part. The Hill tensors are related to Eshelby tensors via equation (2.11). The Eshelby tensor $\mathbb{S}^{\mathrm{esh}}_{\mathrm{sph}}$ corresponding to spherical inclusions (pores in figure 3) reads as

$$\mathbb{S}^{\mathrm{esh}}_{\mathrm{sph}}=\frac{3k_{\mathrm{poly}}}{3k_{\mathrm{poly}}+4\mu_{\mathrm{poly}}}\mathbb{J}+\frac{6(k_{\mathrm{poly}}+2\mu_{\mathrm{poly}})}{5(3k_{\mathrm{poly}}+4\mu_{\mathrm{poly}})}\mathbb{K}. \tag{3.3}$$

In the base frame $(\underline{e}_{\vartheta}, \underline{e}_{\varphi}, \underline{e}_{r})$ $(1=\vartheta, 2=\varphi, 3=r$, see figure 2 for Euler angles $\varphi$ and $\vartheta)$, attached to individual solid discs, the non-zero components of the Eshelby tensor $\mathbb{S}^{\mathrm{esh}}_{\mathrm{disc}}$ corresponding to oblate inclusions read as

$$\left.\begin{aligned} &S^{\mathrm{esh}}_{\mathrm{disc},3333}=1,\\ &S^{\mathrm{esh}}_{\mathrm{disc},3311}=S^{\mathrm{esh}}_{\mathrm{disc},3322}=\frac{\nu_{\mathrm{poly}}}{1-\nu_{\mathrm{poly}}}\\ \text{and}\quad &S^{\mathrm{esh}}_{\mathrm{disc},2323}=S^{\mathrm{esh}}_{\mathrm{disc},3232}=S^{\mathrm{esh}}_{\mathrm{disc},3223}=S^{\mathrm{esh}}_{\mathrm{disc},2332}=S^{\mathrm{esh}}_{\mathrm{disc},3131}\\ &\qquad=S^{\mathrm{esh}}_{\mathrm{disc},1313}=S^{\mathrm{esh}}_{\mathrm{disc},1331}=S^{\mathrm{esh}}_{\mathrm{disc},3113}=\frac{1}{2} \end{aligned}\right\} \tag{3.4}$$

with $\nu_{\mathrm{poly}}$ as Poisson's ratio of the polycrystal,

$$\nu_{\mathrm{poly}}=\frac{3k_{\mathrm{poly}}-2\mu_{\mathrm{poly}}}{6k_{\mathrm{poly}}+2\mu_{\mathrm{poly}}}. \tag{3.5}$$

Following standard tensor calculus (Salencon 2001), the tensor components of $\mathbb{P}^{\mathrm{poly}}_{\mathrm{disc}}(\vartheta,\varphi)=\mathbb{S}^{\mathrm{esh}}_{\mathrm{disc}}(\vartheta,\varphi):\mathbb{C}^{-1}_{\mathrm{poly}}$, being related to differently oriented inclusions, are transformed into one, single base frame $(\underline{e}_1, \underline{e}_2, \underline{e}_3)$, in order to evaluate the integrals in equations (3.1) and (3.2).

### (*b*) *Strength estimate*

Strength of the porous polycrystal made up of HA discs (see figure 3 for its RVE) is related to brittle failure of the most unfavourably stressed single disc. Therefore, the macroscopic stress (and strain) state needs to be related to corresponding stress and strain states in the individual disc-type crystal solid phases. Accordingly, we specify the concentration relations (2.7) and (2.12) for the biomaterial defined through equations (3.1)–(3.5), resulting in

$$\begin{aligned} \boldsymbol{\varepsilon}_{\mathrm{HA}}(\varphi,\vartheta)=&\left[\mathbb{I}+\mathbb{P}^{\mathrm{poly}}_{\mathrm{disc}}(\varphi,\vartheta):(\mathbb{c}_{\mathrm{HA}}-\mathbb{C}_{\mathrm{poly}})\right]^{-1}:\\ &\left\{(1-\phi)\left\langle\left[\mathbb{I}+\mathbb{P}^{\mathrm{poly}}_{\mathrm{disc}}(\varphi,\vartheta):(\mathbb{c}_{\mathrm{HA}}-\mathbb{C}_{\mathrm{poly}})\right]^{-1}\right\rangle\right.\\ &\left.+\,\phi\left(\mathbb{I}-\mathbb{P}^{\mathrm{poly}}_{\mathrm{sph}}:\mathbb{C}_{\mathrm{poly}}\right)^{-1}\right\}^{-1}:\boldsymbol{E}. \end{aligned} \tag{3.6}$$

When applying phase elasticity (2.1) to HA, and overall elasticity (2.6) to the porous biomaterial according to equation (3.1), concentration relation (3.6) can

be recast in terms of stresses

$$\begin{aligned}\boldsymbol{\sigma}_{\mathrm{HA}}(\varphi,\vartheta) = \mathbb{c}_{\mathrm{HA}} : \Bigg\{ & \Big[\mathbb{I} + \mathbb{P}^{\mathrm{poly}}_{\mathrm{disc}}(\varphi,\vartheta) : (\mathbb{c}_{\mathrm{HA}} - \mathbb{C}_{\mathrm{poly}})\Big]^{-1} : \\ & \Big\{(1-\phi)\Big\langle\Big[\mathbb{I} + \mathbb{P}^{\mathrm{poly}}_{\mathrm{disc}}(\varphi,\vartheta) : (\mathbb{c}_{\mathrm{HA}} - \mathbb{C}_{\mathrm{poly}})\Big]^{-1}\Big\rangle \\ & + \phi\Big(\mathbb{I} - \mathbb{P}^{\mathrm{poly}}_{\mathrm{sph}} : \mathbb{C}_{\mathrm{poly}}\Big)^{-1}\Big\}^{-1}\Bigg\} : \mathbb{C}^{-1}_{\mathrm{poly}} : \boldsymbol{\Sigma} \\ = \mathbb{B}_{\mathrm{HA}}(\varphi,\vartheta) : \boldsymbol{\Sigma}, & \end{aligned} \tag{3.7}$$

with $\mathbb{B}_{\mathrm{HA}}(\varphi,\vartheta)$ as the so-called stress concentration tensor of the disc-shaped HA phase with orientation $\underline{e}_r(\varphi,\vartheta)$. We consider that disc failure is governed by the normal stress $\sigma_{\mathrm{HA},NN}(\varphi,\vartheta;\psi)$ acting in the plane of the disc, and by the shear stress acting on planes orthogonal to the disc plane, $\sigma_{\mathrm{HA},Nn}(\varphi,\vartheta;\psi;\omega)$ (see figure 2):

$$\sigma_{\mathrm{HA},NN}(\varphi,\vartheta;\psi) = \underline{N}(\psi)\cdot\boldsymbol{\sigma}_{\mathrm{HA}}(\varphi,\vartheta)\cdot\underline{N}(\psi) \tag{3.8}$$

and

$$\sigma_{\mathrm{HA},Nn}(\varphi,\vartheta;\psi;\omega) = \underline{N}(\psi)\cdot\boldsymbol{\sigma}_{\mathrm{HA}}\cdot\underline{n}(\omega), \tag{3.9}$$

whereby the orientation vector $\underline{N}$ is defined through angle $\psi$ in the plane of the disc (see figure 2 and appendix A for its components in the reference base frame), and direction $\underline{n}$ being orthogonal to $\underline{N}$ and specified through angle $\omega$ (see figure 2 and appendix A for its components in the reference base frame). For the criterion describing failure of one single disc-type solid phase, we consider interaction between tensile strength $\sigma^{\mathrm{ult,t}}_{\mathrm{HA}}$ and shear strength $\sigma^{\mathrm{ult,s}}_{\mathrm{HA}}$, so that this disc-specific failure criterion reads as

$$\begin{aligned} & \vartheta = 0,\ldots,\pi, \quad \psi = 0,\ldots,2\pi, \quad \omega = 0,\ldots,2\pi : \\ & \mathfrak{f}_{\mathrm{HA}}(\boldsymbol{\sigma}) = \max_{\vartheta}\left[\max_{\psi}\left(\beta\max_{\omega}|\sigma_{\mathrm{HA},Nn}| + \sigma_{\mathrm{HA},NN}\right)\right] - \sigma^{\mathrm{ult,t}}_{\mathrm{HA}} = 0 \end{aligned} \tag{3.10}$$

with $\beta = \sigma^{\mathrm{ult,t}}_{\mathrm{HA}}/\sigma^{\mathrm{ult,s}}_{\mathrm{HA}}$ being the ratio between uniaxial tensile strength $\sigma^{\mathrm{ult,t}}_{\mathrm{HA}}$ and the shear strength $\sigma^{\mathrm{ult,s}}_{\mathrm{HA}}$ of pure HA. Use of equations (3.7)–(3.9) in equation (3.10) yields a macroscopic failure criterion in the format of equation (2.14),

$$\begin{aligned}\mathfrak{F}(\boldsymbol{\Sigma}) = \max_{\vartheta}\Bigg\{ & \max_{\psi}\Big[\beta\max_{\omega}|\underline{N}(\psi)\cdot\mathbb{B}_{\mathrm{HA}}(\varphi,\vartheta) : \boldsymbol{\Sigma}\cdot\underline{n}(\omega)| \\ & + \ \underline{N}(\psi)\cdot\mathbb{B}_{\mathrm{HA}}(\varphi,\vartheta) : \boldsymbol{\Sigma}\cdot\underline{N}(\psi)\Big]\Bigg\} - \sigma^{\mathrm{ult,t}}_{\mathrm{HA}} = 0 \end{aligned} \tag{3.11}$$

and a corresponding elastic domain,

$$\mathfrak{F}(\boldsymbol{\Sigma}) < 0 \tag{3.12}$$

Table 2. Universal (biomaterial-independent) isotropic phase properties of pure HA.

| | | |
|---|---|---|
| Young's modulus $E_{HA}$ | 114 GPa | from Katz & Ukraincik (1971) |
| Poisson's ratio $\nu_{HA}$ | 0.27 | from Katz & Ukraincik (1971) |
| uniaxial tensile strength $\sigma_{HA}^{ult,t}$ | 52.2 MPa | from Akao *et al.* (1981) and Shareef *et al.* (1993); see §4*b* for details |
| uniaxial shear strength $\sigma_{HA}^{ult,s}$ | 80.3 MPa | |

with $\mathbb{B}_{HA}$ according to equation (3.7). We will also evaluate the criterion (3.11) for uniaxial macroscopic stress states $\boldsymbol{\Sigma} = \pm\Sigma_{ref}\, \underline{e}_3 \otimes \underline{e}_3$: insertion of these stress states into equation (3.11), while considering equations (3.7)–(3.10), yields an equation for $\Sigma_{ref}$, the corresponding results $\Sigma_{poly}^{ult,t}$ and $\Sigma_{poly}^{ult,c}$ being model predictions of macroscopic uniaxial strengths as functions of (microscopic) crystal strength and biomaterial porosity (see figures 6 and 7, §4 and appendix A for further details).

## 4. Model validation

### (*a*) *Strategy for model validation through independent test data*

In the line of Popper, who stated that a theory—as long as it has not been falsified—will be 'the more satisfactory the greater the severity of independent tests it survives' (cited from Mayr 1997, p. 49), the verification of the micromechanical representation of HA biomaterials (equations (3.1)–(3.5) for elasticity, and equations (3.6)–(3.12) for strength) will rest on two independent experimental sets, as has been successfully done for other material classes such as bone (Hellmich & Ulm 2002; Hellmich *et al.* 2004; Fritsch & Hellmich 2007) or wood (Hofstetter *et al.* 2005, 2006). Biomaterial-specific macroscopic (homogenized) stiffnesses $\mathbb{C}_{poly}$ (Young's moduli $E_{poly}$ and Poisson's ratios $\nu_{poly}$), and uniaxial (tensile and compressive) strengths ($\Sigma_{poly}^{ult,t}$ and $\Sigma_{poly}^{ult,c}$), predicted by the micromechanics model (3.1)–(3.12) on the basis of biomaterial-independent (universal) elastic and strength properties of pure HA (experimental set I, table 2) for biomaterial-specific porosities $\phi$ (experimental set IIa, tables 3 and 4), are compared with corresponding biomaterial-specific experimentally determined moduli $E_{exp}$ and Poisson's ratios $\nu_{exp}$ (experimental set IIb-1, table 3) and uniaxial tensile/compressive strength values (experimental set IIb-2, table 4). Because we avoided introduction of micromorphological features that cannot be experimentally quantified (such as the precise crystal shape), all material parameters are directly related to well-defined experiments.

### (*b*) *Universal mechanical properties of (biomaterial-independent) HA—experimental set I*

Experiments with an ultrasonic interferometer coupled with a solid media pressure apparatus (Katz & Ukraincik 1971; Gilmore & Katz 1982) reveal the isotropic elastic constants of dense HA powder ($\phi = 0$), Young's modulus $E_{HA} = 114$ GPa, and Poisson's ratio $\nu_{HA} = 0.27$ (equivalent to bulk modulus $k_{HA} = E_{HA}/3/(1 - 2\nu_{HA}) = 82.6$ GPa and shear modulus $\mu_{HA} = E_{HA}/2/(1 + \nu_{HA}) = 44.9$ GPa).

Table 3. Experimental Young's modulus $E_{\mathrm{exp}}$ and Poisson's ratio $\nu_{\mathrm{exp}}$ of HA biomaterials, as a function of porosity $\phi$.

| reference | $\phi$ (%) | $E_{\mathrm{exp}}$ (GPa) | $\nu_{\mathrm{exp}}$ |
|---|---|---|---|
| Akao *et al.* (1981) | 2.8 | 88 | |
| | 3.9 | 85 | |
| | 9.1 | 80 | |
| | 19.4 | 44 | |
| de With *et al.* (1981) | 3 | 112 | 0.275 |
| | 6 | 103 | 0.272 |
| | 9 | 93 | 0.265 |
| | 17 | 78 | 0.253 |
| | 22 | 67 | 0.242 |
| | 27 | 54 | 0.238 |
| Arita *et al.* (1995) | 6 | 88 | |
| | 28 | 41 | |
| | 33 | 32 | |
| | 35 | 29 | |
| | 50 | 14 | |
| | 52 | 10 | |
| Liu (1998) | 8 | 93 | |
| | 17 | 78 | |
| | 21 | 66 | |
| | 32 | 44 | |
| | 44 | 22 | |
| | 54 | 18 | |
| Charrière *et al.* (2001) | 44 | 13.5 | |

The authors are not aware of direct strength tests on pure HA (with $\phi = 0$). Therefore, we consider one uniaxial tensile test, $\Sigma_{\mathrm{exp}}^{\mathrm{ult,t}} = 37.1\,\mathrm{MPa}$, and one uniaxial compressive test, $\Sigma_{\mathrm{exp}}^{\mathrm{ult,c}} = 509\,\mathrm{MPa}$, on fairly dense samples (with $\phi = 12.2\%$ and 2.8%, respectively), conducted by Shareef *et al.* (1993) and Akao *et al.* (1981), respectively (table 4). From these two tests, we back-calculate, via evaluation of equations (3.7)–(3.11) for $\boldsymbol{\Sigma} = \Sigma_{\mathrm{exp}}^{\mathrm{ult,t}}\, \underline{e}_3 \otimes \underline{e}_3$ and $\boldsymbol{\Sigma} = -\Sigma_{\mathrm{exp}}^{\mathrm{ult,c}}\, \underline{e}_3 \otimes \underline{e}_3$, the universal tensile and shear strength of pure HA, $\sigma_{\mathrm{HA}}^{\mathrm{ult,t}}$ and $\sigma_{\mathrm{HA}}^{\mathrm{ult,s}}$ (table 2).

### (*c*) *Biomaterial-specific porosities—experimental set IIa*

Porosity of HA biomaterials is standardly calculated from mass $M$ and volume $V$ of well-defined samples on the basis of the mass density of pure HA, $\rho_{\mathrm{HA}} = 3.16\,\mathrm{g\,cm^{-3}}$ (Dorozhkin & Epple 2002),

$$\phi = 1 - \frac{M}{V \rho_{\mathrm{HA}}}. \tag{4.1}$$

Corresponding porosity values have been reported by different investigators (Peelen *et al.* 1978; Akao *et al.* 1981; de With *et al.* 1981; Shareef *et al.* 1993; Arita *et al.* 1995; Martin & Brown 1995; Liu 1998; Charrière *et al.* 2001), see tables 3 and 4.

Table 4. Experimental compressive strength $\Sigma_{\mathrm{exp}}^{\mathrm{ult,c}}$ and tensile strength $\Sigma_{\mathrm{exp}}^{\mathrm{ult,t}}$ of HA biomaterials, as functions of porosity $\phi$.

| reference | $\phi$ (%) | $\Sigma_{\mathrm{exp}}^{\mathrm{ult,c}}$ (MPa) | $\Sigma_{\mathrm{exp}}^{\mathrm{ult,t}}$ (MPa) |
|---|---|---|---|
| Peelen *et al.* (1978) | 36 | 160 | |
| | 48 | 114 | |
| | 60 | 69 | |
| | 65 | 45 | |
| | 70 | 30 | |
| Akao *et al.* (1981) | 2.8 | 509 | |
| | 3.9 | 465 | |
| | 9.1 | 415 | |
| | 19.4 | 308 | |
| Shareef *et al.* (1993) | 12.2 | | 37.1 |
| | 16.1 | | 32.8 |
| | 20.6 | | 31.8 |
| | 24.8 | | 24.2 |
| | 27.3 | | 23.6 |
| | 29.2 | | 20.0 |
| Martin & Brown (1995) | 27.0 | 172.5 | |
| | 39.0 | 119.0 | |
| Liu (1998) | 20.2 | | 25.5 |
| | 26.8 | | 20.0 |
| | 29.0 | | 16.8 |
| | 32.6 | | 13.9 |
| | 39.6 | | 14.4 |
| | 42.8 | | 11.1 |
| | 50.9 | | 7.2 |
| | 54.5 | | 8.0 |

### (*d*) *Biomaterial-specific elasticity experiments on HA biomaterials—experimental set IIb-1*

Elastic properties of HA biomaterials were determined through uniaxial quasi-static mechanical tests (Akao *et al.* 1981; Charrière *et al.* 2001), but also through ultrasonic techniques (de With *et al.* 1981; Liu 1998), or resonance frequency tests (Arita *et al.* 1995).

In uniaxial quasi-static experiments, the gradient of the stress–strain curve gives access to Young's modulus. Respective experimental results are documented for cuboidal specimens (Akao *et al.* 1981) and hollow cylindrical specimens (Charrière *et al.* 2001), see table 3 and figure 4.

In ultrasonic experiments (Ashman *et al.* 1984, 1987), the time of flight of an ultrasonic wave travelling through the specimen with a certain frequency $f$ is measured. The calculated velocity of the wave, $v$, together with material mass density of the sample, gives access to the elastic constants (Kolsky 1953; Carcione 2001). Because the ultrasonic wavelength $\lambda$, $\lambda = v/f$, is a measure for the loading of the structure ($\lambda \approx \mathcal{L}$ in figure 1), the mechanical properties are related to an RVE

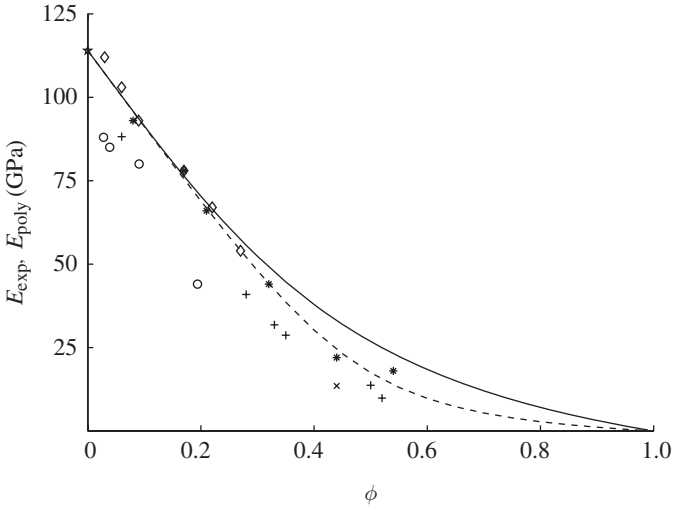


Figure 4. Comparison between model predictions ($E_{poly}$; equations (3.1)–(3.5)) and experiments ($E_{exp}$) for Young's modulus of different porous biomaterials made of HA, as a function of porosity $\phi$. Unfilled circle, exp-static: Akao *et al.* (1981); diamond, exp-ultra: de With *et al.* (1981); star, exp-ultra: Gilmore & Katz (1982); plus, exp-res: Arita *et al.* (1995); asterisk, exp-ultra: Liu (1998); cross, exp-static: Charriére *et al.* (2001); solid line, disc model; dashed line, needle model (ultra, ultrasonic tests; res, resonance frequency tests; static, quasi-static uniaxial tests).

with characteristic length $\ell \ll \lambda$. Respective experimental results are documented for bar-shaped specimens (Liu 1998) and cylindrical samples (de With *et al.* 1981), see table 4 and figures 4 and 5.

In resonance frequency tests (Schreiber *et al.* 1973), beam type specimens are excited in the flexural vibration mode, and the corresponding free vibration gives access to the fundamental resonance frequency. The latter allows for determination, via the mass density and the geometry of the sample, of Young's modulus of the sample. Respective experimental results are documented for disc-shaped biomaterial samples (Arita *et al.* 1995), see table 3 and figure 4.

### (*e*) *Comparison between biomaterial-specific stiffness predictions and corresponding experiments*

The stiffness values predicted by the homogenization scheme (3.1)–(3.5) (see §3 and figure 3) for biomaterial-specific porosities (§4*c*, experimental set IIa) on the basis of biomaterial-independent (universal) stiffness of HA (§4*b*, experimental set I) are compared with corresponding experimentally determined biomaterial-specific stiffness values from experimental set IIb-1 (§4*d*). To quantify the model's predictive capabilities, we consider the mean and the standard deviation of the absolute error $\mathcal{E}$ between stiffness predictions and experiments,

$$\bar{\mathcal{E}} = \frac{1}{n}\sum_{i=1}^{n} \mathcal{E}_i = \frac{1}{n}\sum_{i=1}^{n} q_i^{\mathrm{pred}} - q_i^{\mathrm{exp}} \tag{4.2}$$

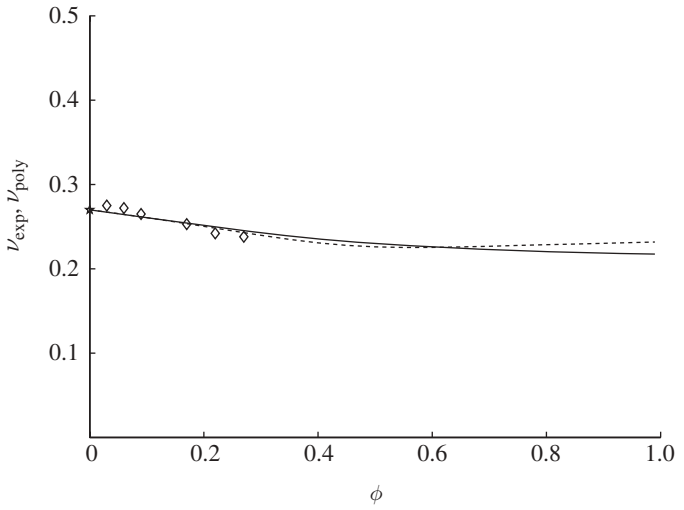


Figure 5. Comparison between model predictions ($\nu_{poly}$; equations (3.1)–(3.5)) and experiments ($\nu_{exp}$) for Poisson's ratio of different porous biomaterials made of HA, as a function of porosity $\phi$. Diamond, exp-ultra: de With *et al.* (1981); star, exp-ultra: Gilmore & Katz (1982); solid line, disc model; dashed line, needle model (ultra, ultrasonic tests).

and

$$\mathcal{E}_S = \left[ \frac{1}{n-1} \sum_{i=1}^{n} (\mathcal{E}_i - \bar{\mathcal{E}})^2 \right]^{1/2}, \tag{4.3}$$

where $q$ has to be replaced by the quantity in question, $E$ or $\nu$, and with summation over $n$ stiffness values (tables 3 and 4). These error measures are normalized with respect to the mean value of all experimental data,

$$\bar{q}_{exp} = \frac{1}{n} \sum_{i=1}^{n} q_i^{exp}, \tag{4.4}$$

yielding the error measures $\bar{e}$ and $e_S$ in the form

$$\bar{e} = \frac{\bar{\mathcal{E}}}{\bar{q}_{exp}} \quad \text{and} \quad e_S = \frac{\mathcal{E}_S}{\bar{q}_{exp}}. \tag{4.5}$$

Insertion of biomaterial-specific porosities (table 3) into equation (3.1) delivers, together with equations (3.2)–(3.5), the biomaterial-specific stiffness estimates for the effective Young's modulus $E_{poly}$ and the effective Poisson's ratio $\nu_{poly}$. These stiffness predictions are compared with corresponding experimental stiffness values (figures 4 and 5). We observe a certain overestimation of experimental stiffnesses for porosities larger than 0.4 (figure 4), quantified through overall prediction errors of $15.3 \pm 15.2\%$ (mean value $\pm$ standard deviation according to equation (4.5)), while Poission's ratios are virtually perfectly predicted ($-0.2 \pm 2.7\%$; see figure 5).

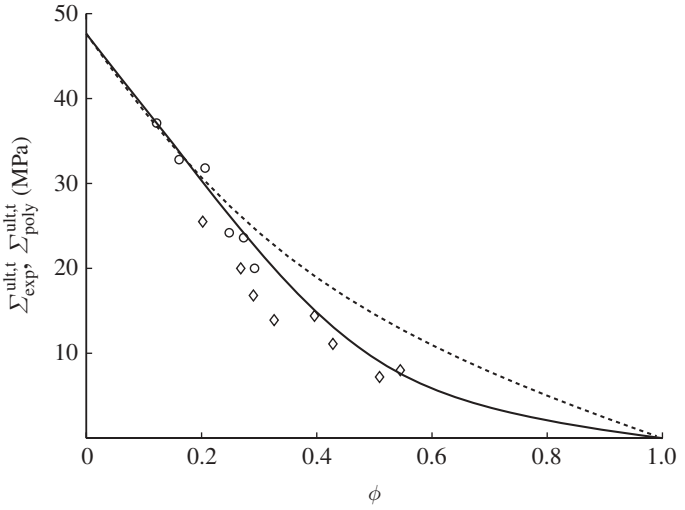


Figure 6. Comparison between model predictions (equations (3.1)–(3.11)) and experiments for tensile strength of different porous biomaterials made of HA, as a function of porosity $\phi$. Circle, exp: Shareef *et al.* (1993); diamond, exp: Liu (1998); dashed line, disc model; solid line, needle model.

### (*f*) *Biomaterial-specific strength experiments on HA biomaterials (experimental set IIb-2)*

In uniaxial compressive quasi-static tests, a sharp decrease of stress after a stress peak in the stress–strain diagram (Akao *et al.* 1981; Martin & Brown 1995) indicates brittle material failure, as observed for all biomaterials described herein, and the aforementioned stress peak is referred to as the ultimate stress or uniaxial strength $\Sigma^{ult,c}_{exp}$. Respective experimental results are documented for cylindrical samples (Peelen *et al.* 1978) and bars (Akao *et al.* 1981), see table 4 and figure 7.

In three-point bending tests, a force $F_s$ is applied to the centre of a beam specimen, and the maximum normal stress $\boldsymbol{\Sigma}^{ult} = \Sigma^{ult}\,\underline{e}_3 \otimes \underline{e}_3$ in the bar-type sample is calculated according to beam theory as

$$\Sigma^{ult,t}_{exp} = \frac{3F_s l_s}{2b_s h_s^2}, \tag{4.6}$$

with $l_s$, $b_s$ and $h_s$ as the length, width and height of the specimen with rectangular cross-section, respectively. Respective experimental results (Liu 1998) are depicted in table 4 and in figure 6.

In the Stanford ring bursting test, ring-shaped specimens are pressurized internally, in order to generate a tensile hoop stress in the ring. The pressure is increased until the sample fails. The tensile stress in the ring is calculated according to

$$\Sigma^{ult,t}_{exp} = \frac{r_s p_i}{d_s}, \tag{4.7}$$

with $r_s$ as the inner diameter of the ring, $p_i$ as the internal pressure and $d_s$ as the wall thickness of the ring. Respective experimental results (Shareef *et al.* 1993) are depicted in table 4 and figure 6.

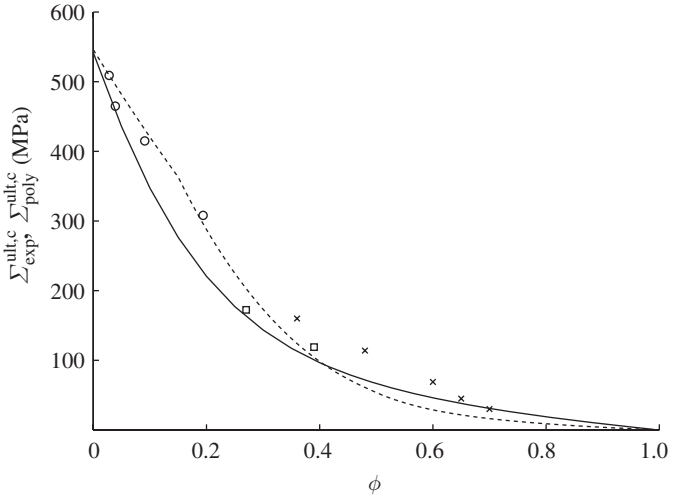


Figure 7. Comparison between model predictions (equations (3.1)–(3.11)) and experiments for compressive strength of different porous biomaterials made of HA, as a function of porosity $\phi$. Cross, exp: Peelen *et al.* (1978); circle, exp: Akao *et al.* (1981); square, exp: Martin & Brown (1995); solid line, disc model; dashed line, needle model.

### (*g*) *Comparison between biomaterial-specific strength predictions and corresponding experiments*

The strength values predicted by upscaling relation (3.11), together with equations (3.7)–(3.10) and (3.3)–(3.5), see §3 and figure 3, for biomaterial-specific porosities (§4*c*, experimental set IIa) on the basis of biomaterial-independent (universal) uniaxial tensile and compressive strengths of HA (§4*b*, experimental set I) are compared with corresponding experimentally determined biomaterial-specific uniaxial tensile and compressive strength values from experimental set IIb-2 (§4*f*).

Insertion of biomaterial-specific porosities (table 4) into equation (3.11), together with equations (3.7)–(3.10) and (3.3)–(3.5), delivers, together with $E_{\mathrm{HA}}$, $\nu_{\mathrm{HA}}$, $\sigma^{\mathrm{ult,t}}_{\mathrm{HA}}$ and $\sigma^{\mathrm{ult,s}}_{\mathrm{HA}}$ (table 2), biomaterial-specific strength estimates for uniaxial tensile strength ($\Sigma^{\mathrm{ult,t}}_{\mathrm{poly}}$) and uniaxial compressive strength ($\Sigma^{\mathrm{ult,c}}_{\mathrm{poly}}$). These strength predictions are compared with corresponding experimental strength values (figures 6 and 7). We observe a certain overestimation of experimental tensile strength for porosities larger than 0.4, which is quantified through error measures of $24.2 \pm 15.2\%$ (mean value $\pm$ standard deviation), while the predictions of the biomaterials' compressive strengths are remarkably better ($-14.5 \pm 13.5\%$).

## 5. Discussion of model features—comparison with needle-based models

It is interesting to evaluate the spatial orientation of the disc-shaped crystal phases initiating overall failure by fulfilling local failure criterion (3.10), measured through critical angle $\vartheta_{\mathrm{cr}}$ from the macroscopic loading direction $\underline{e}_3$, for tensile and compressive uniaxial macroscopic loading, as a function of porosity

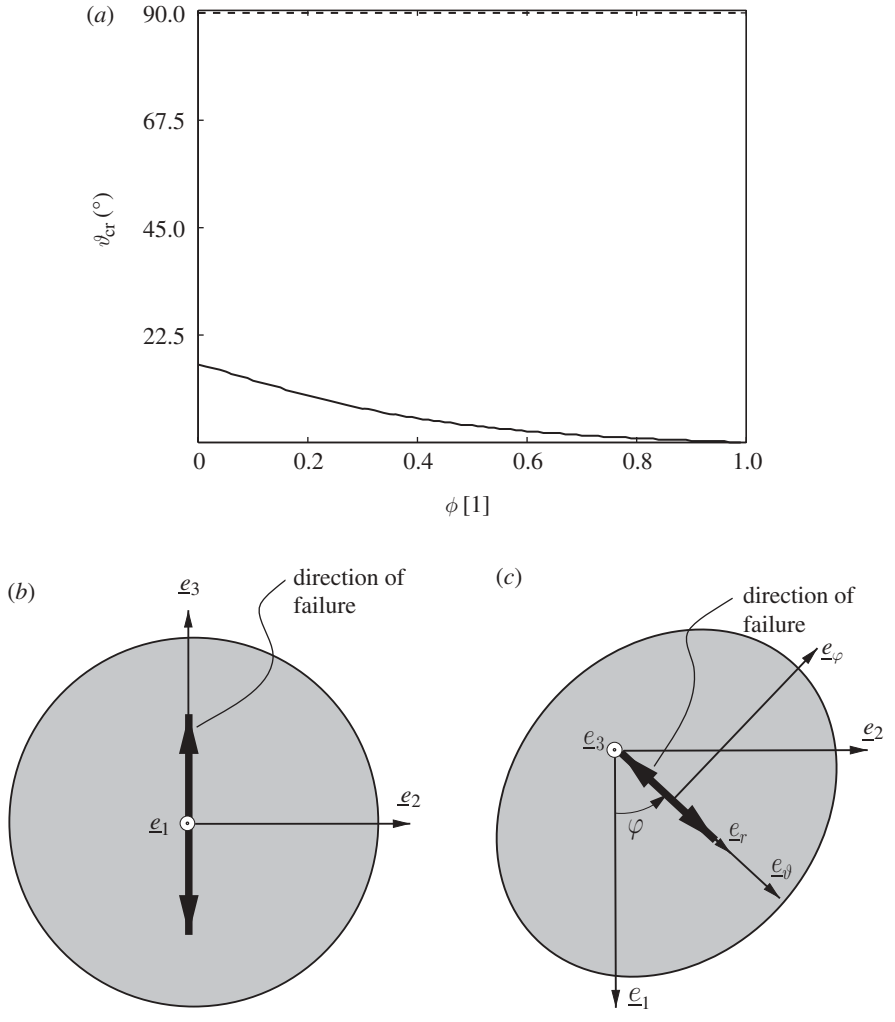


Figure 8. (*a*) Orientation of crystal disc initiating overall failure by fulfilling local failure criterion (3.10), measured through critical angle $\vartheta_{cr}$ from the loading direction, for tensile (dashed line) and compressive (solid line) uniaxial macroscopic loading, as a function of porosity $\phi$; (*b*) typical disc-shaped crystal phase failing under uniaxial tension (macroscopic loading direction $\underline{e}_3$); (*c*) typical disc-shaped crystal phase failing under uniaxial compression (macroscopic loading direction $\underline{e}_3$).

$\phi$—together with the critical stresses occurring then in these phases (figures 8 and 9). Under tensile uniaxial macroscopic loading, failure occurs in crystal discs with normals $\underline{e}_r$ being oriented exactly perpendicular to the macroscopic loading direction ($\vartheta_{cr} = \pi/2$, see dashed line in figure 8*a*), for the entire range of biomaterial porosities. Within these failure-governing disc-shaped crystal phases, the maximum critical stress ($\beta \max_\omega |\sigma_{HA,Nn}| + \sigma_{HA,NN}$, compare equation (3.10)) occurs at angle $\psi = 0$, i.e. exactly in the macroscopic loading direction (see figure 8*b*). In contrast, compressive uniaxial macroscopic loading induces failure in disc-shaped crystals with normals being oriented closely to the loading direction,

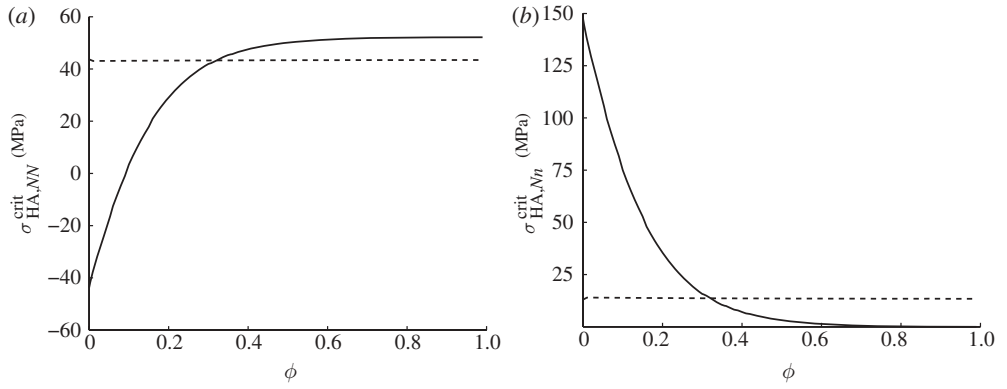


Figure 9. Stress state in disc-shaped crystal phases fulfilling local failure criterion (3.10), in terms of (*a*) normal stresses and of (*b*) shear stresses in planes perpendicular to the direction of normal stress, for tensile (dashed line) and compressive (solid line) uniaxial macroscopic loading, as a function of porosity $\phi$.

and the more so the higher the porosity ($16^\circ \geq \vartheta_{\mathrm{cr}} \geq 0$, see solid line in figure 8*a*). Within these failure-inducing, disc-shaped crystal phases, the maximum critical stress ($\beta \max_\omega |\sigma_{\mathrm{HA},Nn}| + \sigma_{\mathrm{HA},NN}$, compare equation (3.10)) occurs again at angles $\psi = 0$ (or $\psi = \pi$), i.e. the critical direction belongs to planes through the macroscopic loading axis (figure 8*c*). As regards the crystal stresses at failure, normal tensile stresses in the failing disc phase prevail under tensile macroscopic loading (see dashed line in figure 9*a*), while the shear stresses in the failing disc phase are much smaller (see dashed line in figure 9*b*). In contrast, both tensile and compressive normal stresses may occur under uniaxial compressive macroscopic stress states, the former for porosities higher than 10 per cent, the latter for porosities lower than 10 per cent (see solid line in figure 9*a*). These normal stresses are accompanied by shear stresses, starting from a very high level for zero porosity, and decreasing with increasing porosities, finally reaching zero for 100 per cent porosity (see solid line in figure 9*b*).

It is also illustrative to compare our crystal disc-based model predictions with our earlier crystal needle-based predictions (see figures 4–7): while both morphologies lead to satisfactory predictions, it seems noteworthy that, as a rule, the present crystal disc-based model turns out to deliver equally or less satisfactory predictions than the earlier needle-based model. This can be quantified through comparison of relative error measures: $15.3 \pm 15.2\%$ (disc) versus $9.7 \pm 14.7\%$ (needle) for Young's modulus; $-0.2 \pm 2.7\%$ (disc) versus $-0.5 \pm 2.3\%$ (needle) for Poisson's ratio; and $-14.5 \pm 13.5\%$ (disc) versus $-5.6 \pm 16.1\%$ (needle) for compressive strength (figure 7). Hence, we might conclude that, unless more detailed information on the actual crystal shape is available, our previously proposed crystal needle-based micromechanics model for prediction of elasticity and strength of HA biomaterials might be regarded as favourable choice. However, the more relevant conclusion probably is that, once clearly non-spherical crystal shape is considered (be it the needle or the disc-like limit case), a self-consistent continuum micromechanics formulation can satisfactorily predict elasticity and brittle strength of HA biomaterials.

## Appendix A. Global coordinates of vectors $\underline{N}$ and $\underline{n}$

Following standard rules of tensor calculus, each of equations (3.6)–(3.11) needs to be evaluated in one base frame system, e.g. the reference base frame ($\underline{e}_1$, $\underline{e}_2$, $\underline{e}_3$). In this context, we shortly recall the components of $\underline{N}$ and $\underline{n}$ in the reference base frame ($\underline{e}_1$, $\underline{e}_2$, $\underline{e}_3$). Therefore, we first give the components of base vectors of the disc-specific frame ($\underline{e}_\vartheta$, $\underline{e}_\varphi$, $\underline{e}_r$) in the reference base frame ($\underline{e}_1$, $\underline{e}_2$, $\underline{e}_3$):

$$\left.\begin{aligned} \underline{e}_\vartheta &= \cos\varphi\cos\vartheta\,\underline{e}_1 + \sin\varphi\cos\vartheta\,\underline{e}_2 - \sin\vartheta\,\underline{e}_3,\\ \underline{e}_\varphi &= -\sin\varphi\,\underline{e}_1 + \cos\varphi\,\underline{e}_2 \\ \text{and}\qquad \underline{e}_r &= \cos\varphi\sin\vartheta\,\underline{e}_1 + \sin\varphi\sin\vartheta\,\underline{e}_2 + \cos\vartheta\,\underline{e}_3. \end{aligned}\right\} \tag{A 1}$$

In the spherical coordinate system ($\underline{e}_\vartheta$, $\underline{e}_\varphi$, $\underline{e}_r$) (see figure 2), the normal vector $\underline{N}$ has the components

$$\underline{N} = \cos\psi\,\underline{e}_\vartheta + \sin\psi\,\underline{e}_\varphi. \tag{A 2}$$

Hence, its components in the reference coordinate frame read as

$$\begin{aligned} \underline{N} = {} & (\cos\psi\cos\varphi\cos\vartheta - \sin\psi\sin\varphi)\,\underline{e}_1 \\ & + (\cos\psi\sin\varphi\cos\vartheta + \sin\psi\cos\varphi)\,\underline{e}_2 - \cos\psi\sin\vartheta\,\underline{e}_3. \end{aligned} \tag{A 3}$$

$\underline{N} = \underline{e}'_3$ is chosen as one vector of a new base frame attached to the disc under investigation, ($\underline{e}'_1$, $\underline{e}'_2$, $\underline{e}'_3$) (figure 2). This new base frame is related to the reference base through Euler angles $\varphi'$ and $\vartheta'$, reading as

$$\varphi' = \arctan\left(\frac{\cos\psi\sin\varphi\cos\vartheta + \sin\psi\cos\varphi}{\cos\psi\cos\varphi\cos\vartheta - \sin\psi\sin\varphi}\right) \tag{A 4}$$

and

$$\vartheta' = \arccos(-\cos\psi\sin\vartheta). \tag{A 5}$$

The angles $\vartheta'$ and $\varphi'$ give access to the reference frame-related coordinates of $\underline{e}'_1$ and $\underline{e}'_2$,

$$\left.\begin{aligned} \underline{e}'_1 &= \cos\varphi'\cos\vartheta'\,\underline{e}_1 + \sin\varphi'\cos\vartheta'\,\underline{e}_2 - \sin\vartheta'\,\underline{e}_3\\ \text{and}\qquad \underline{e}'_2 &= -\sin\varphi'\,\underline{e}_1 + \cos\varphi'\,\underline{e}_2. \end{aligned}\right\} \tag{A 6}$$

Finally, the reference frame-related coordinates $\underline{e}'_1$ and $\underline{e}'_2$ give, via $\omega$ (figure 2), access to the reference frame-related coordinates of normal $\underline{n}$,

$$\begin{aligned} \underline{n} &= \cos\omega\,\underline{e}'_1 + \sin\omega\,\underline{e}'_2 \\ &= (\cos\omega\cos\varphi'\cos\vartheta' - \sin\omega\sin\varphi')\,\underline{e}_1 \\ &\quad + (\cos\omega\sin\varphi'\cos\vartheta' + \sin\omega\cos\varphi')\,\underline{e}_2 - \cos\omega\sin\vartheta'\,\underline{e}_3. \end{aligned} \tag{A 7}$$

## References

Akao, M., Aoki, H. & Kato, K. 1981 Mechanical properties of sintered hydroxyapatite for prosthetic applications. *J. Mater. Sci.* **16**, 809–812. (doi:10.1007/BF02402799)

Arita, I. H., Wilkinson, D. S., Mondragón, M. A. & Castaño, V. M. 1995 Chemistry and sintering behaviour of thin hydroxyapatite ceramics with controlled porosity. *Biomaterials* **16**, 403–408. (doi:10.1016/0142-9612(95)98858-B)

Ashman, R. B., Cowin, S. C., van Buskirk, W. C. & Rice, J. C. 1984 A continuous wave technique for the measurement of the elastic properties of cortical bone. *J. Biomech.* **17**, 349–361. (doi:10.1016/0021-9290(84)90029-0)

Ashman, R. B., Corin, J. D. & Turner, C. H. 1987 Elastic properties of cancellous bone: measurement by an ultrasonic technique. *J. Biomech.* **20**, 979–986. (doi:10.1016/0021-9290(87)90327-7)

Benveniste, Y. 1987 A new approach to the application of Mori–Tanaka's theory in composite materials. *Mech. Mater.* **6**, 147–157. (doi:10.1016/0167-6636(87)90005-6)

Cancedda, R., Cedola, A., Giuliani, A., Komlev, V., Lagomarsino, S., Mastrogiacomo, M., Peyrin, F. & Rustichelli, F. 2007 Bulk and interface investigations of scaffolds and tissue-engineered bones by X-ray microtomography and X-ray microdiffraction. *Biomaterials* **28**, 2505–2524. (doi:10.1016/j.biomaterials.2007.01.022)

Carcione, J. M. 2001 *Wave fields in real media: wave propagation in anisotropic, anelastic and porous media*. Oxford, UK: Pergamon.

Charrière, E., Terrazzoni, S., Pittet, C., Mordasini, Ph., Dutoit, M., Lemaître, J. & Zysset, Ph. 2001 Mechanical characterization of brushite and hydroxyapatite cements. *Biomaterials* **22**, 2937–2945. (doi:10.1016/S0142-9612(01)00041-2)

Cowin, S. C. 2003 A recasting of anisotropic poroelasticity in matrices of tensor components. *Trans. Porous Media* **50**, 35–56. (doi:10.1023/A:1020626717067)

Cowin, S. C. & Mehrabadi, M. M. 1992 The structure of the linear anisotropic elastic symmetries. *J. Mech. Phys. Solids* **40**, 1459–1471. (doi:10.1016/0022-5096(92)90029-2)

de With, G., van Dijk, H. J. A., Hattu, N. & Prijs, K. 1981 Preparation, microstructure and mechanical properties of dense polycrystalline hydroxy apatite. *J. Mater. Sci.* **16**, 1592–1598. (doi:10.1007/BF02396876)

Dorozhkin, S. V. & Epple, M. 2002 Biological and medical significance of calcium phosphates. *Angew. Chem. Int. Ed.* **41**, 3130–3146.

Eshelby, J. D. 1957 The determination of the elastic field of an ellipsoidal inclusion, and related problems. *Proc. R. Soc. Lond. A* **241**, 376–396. (doi:10.1098/rspa.1957.0133)

Fritsch, A. & Hellmich, Ch. 2007 'Universal' microstructural patterns in cortical and trabecular, extracellular and extravascular bone materials: micromechanics-based prediction of anisotropic elasticity. *J. Theor. Biol.* **244**, 597–620. (doi:10.1016/j.jtbi.2006.09.013)

Fritsch, A., Dormieux, L. & Hellmich, Ch. 2006 Porous polycrystals built up by uniformly and axisymmetrically oriented needles: homogenization of elastic properties. *Compt. Rend. Méc.* **334**, 151–157. (doi:10.1016/j.crme.2006.01.008)

Fritsch, A., Dormieux, L., Hellmich, Ch. & Sanahuja, J. 2007 Micromechanics of crystal interfaces in polycrystalline solid phases of porous media: fundamentals and application to strength of hydroxyapatite biomaterials. *J. Mater. Sci.* **42**, 8824–8837. (doi:10.1007/s10853-007-1859-4)

Fritsch, A., Dormieux, L., Hellmich, Ch. & Sanahuja, J. 2009 Mechanical behaviour of hydroxyapatite biomaterials: an experimentally validated micromechanical model for elasticity and strength. *J. Biomed. Mater. Res. A* **88A**, 149–161. (doi:10.1002/jbm.a.31727)

Gilmore, R. S. & Katz, J. L. 1982 Elastic properties of apatites. *J. Mater. Sci.* **17**, 1131–1141. (doi:10.1007/BF00543533)

Hashin, Z. 1983 Analysis of composite materials: a survey. *J. Appl. Mech.* **50**, 481–505. (doi:10.1115/1.3167081)

Hellmich, Ch. & Ulm, F.-J. 2002 A micromechanical model for the ultrastructural stiffness of mineralized tissues. *J. Eng. Mech.* (*ASCE*) **128**, 898–908. (doi:10.1061/(ASCE)0733-9399(2002)128:8(898))

Hellmich, Ch., Barthélémy, J.-F. & Dormieux, L. 2004 Mineral–collagen interactions in elasticity of bone ultrastructure—a continuum micromechanics approach. *Eur. J. Mech. A Solids* **23**, 783–810. (doi:10.1016/j.euromechsol.2004.05.004)

Helnwein, P. 2001 Some remarks on the compressed matrix representation of symmetric second-order and fourth-order tensors. *Comp. Meth. Appl. Mech. Eng.* **190**, 2753–2770. (doi:10.1016/S0045-7825(00)00263-2)

Hershey, A. V. 1954 The elasticity of an isotropic aggregate of anisotropic cubic crystals. *J. Appl. Mech.* (*ASME*) **21**, 236–240.

Hill, R. 1963 Elastic properties of reinforced solids: some theoretical principles. *J. Mech. Phys. Solids* **11**, 357–362. (doi:10.1016/0022-5096(63)90036-X)

Hofstetter, K., Hellmich, Ch. & Eberhardsteiner, J. 2005 Development and experimental validation of a continuum micromechanics model for the elasticity of wood. *Eur. J. Mech. A Solids* **24**, 1030–1053. (doi:10.1016/j.euromechsol.2005.05.006)

Hofstetter, K., Hellmich, C. & Eberhardsteiner, J. 2006 The influence of the microfibril angle on wood stiffness: a continuum micromechanics approach. *Comp. Assist. Mech. Eng. Sci.* **13**, 523–536.

Katz, J. K. & Ukraincik, K. 1971 On the anisotropic elastic properties of hydroxyapatite. *J. Biomech.* **4**, 221–227. (doi:10.1016/0021-9290(71)90007-8)

Kolsky, H. 1953 *Stress waves in solids*. Oxford, UK: Clarendon Press.

Kröner, E. 1958 Computation of the elastic constants of polycrystals from constants of single crystals. *Z. Phys.* **151**, 504–518. [In German.]

Lacroix, D., Chateau, A., Ginebra, M.-P. & Planell, J. A. 2006 Micro-finite element models of bone tissue-engineering scaffolds. *Biomaterials* **27**, 5326–5334. (doi:10.1016/j.biomaterials.2006.06.009)

Laws, N. 1977 The determination of stress and strain concentrations at an ellipsoidal inclusion in an anisotropic material. *J. Elasticity* **7**, 91–97. (doi:10.1007/BF00041133)

Liu, D.-M. 1998 Preparation and characterisation of porous hydroxyapatite bioceramic via a slip-casting route. *Ceram. Int.* **24**, 441–446. (doi:10.1016/S0272-8842(97)00033-3)

Malasoma, A., Fritsch, A., Kohlhauser, Ch., Brynk, T., Vitale-Brovarone, C., Pakiela, Z., Eberhardsteiner, J. & Hellmich, Ch. 2008 Micromechanics of bioresorbable porous CEL2 glass–ceramic scaffolds for bone tissue engineering. *Adv. Appl. Ceram.* **107**, 277–286. (doi:10.1179/174367508X306488)

Martin, R. I. & Brown, P. W. 1995 Mechanical properties of hydroxyapatite formed at physiological temperature. *J. Mater. Sci. Mater. Med.* **6**, 138–143. (doi:10.1007/BF00120289)

Mayr, E. 1997 *This is biology—the science of the living world*, 1st edn. Cambridge, MA: Harvard University Press.

Mori, T. & Tanaka, K. 1973 Average stress in matrix and average elastic energy of materials with misfitting inclusions. *Acta Metal.* **21**, 571–574. (doi:10.1016/0001-6160(73)90064-3)

Peelen, J. G. J., Rejda, B. V. & de Groot, K. 1978 Preparation and properties of sintered hydroxylapatite. *Ceram. Int.* **4**, 71–74.

Pereira, M. M., Jones, J. R. & Hench, L. L. 2005 Bioactive glass and hybrid scaffolds prepared by sol-gel method for bone tissue engineering. *Adv. Appl. Ceram.* **104**, 35–42. (doi:10.1179/174367605225011034)

Salencon, J. 2001 *Handbook of continuum mechanics—general concepts. Thermoelasticity*. Berlin, Germany: Springer.

Scheiner, S., Sinibaldi, R., Pichler, B., Komlev, V., Renghini, C., Vitale-Brovarone, C., Rustichelli, F. & Hellmich, Ch. 2009 Micromechanics of bone tissue-engineering scaffolds, based on resolution error-cleared computer tomography. *Biomaterials* **30**, 2411–2419. (doi:10.1016/j.biomaterials.2008.12.048)

Schreiber, E., Anderson, O. L. & Soga, N. 1973 *Elastic constants and their measurement*. New York, NY: McGraw-Hill.

Shareef, M. Y., Messer, P. F. & van Noort, R. 1993 Fabrication, characterization and fracture study of a machinable hydroxyapatite ceramic. *Biomaterials* **14**, 69–75. (doi:10.1016/0142-9612(93)90078-G)

Suquet, P. (ed.) 1997 *Continuum micromechanics*. Vienna, Austria; New York, NY: Springer.

Zaoui, A. 2002 Continuum micromechanics: survey. *J. Eng. Mech.* (*ASCE*) **128**, 808–816. (doi:10.1061/(ASCE)0733-9399(2002)128:8(808))